An asymmetric sodium extraction/insertion mechanism for the Fe/V-Mixed NASICON Na4FeV(PO4)3

Sunkyu Park, Jean-Noël Chotard, Dany Carlier, Iona Moog, Mathieu Duttine, François Fauth, Antonella Iadecola, Laurence Croguennec, Christian Masquelier

HAL Id: hal-03671793
https://hal.science/hal-03671793

Submitted on 18 May 2022

An asymmetric Sodium Extraction/Insertion Mechanism for the Fe/V-mixed NASICON Na$_4$FeV(PO$_4$)$_3$

Sunkyu Park [1,2,3], Jean-Noël Chotard [1,5], Dany Carlier [2,5], Iona Moog [3], Mathieu Duttine [2], François Fauth [4], Antonella Iadecola [5], Laurence Croguennec [*,2,5] and Christian Masquelier [*,1,5]

[1] *Laboratoire de Réactivité et de Chimie des Solides, Université de Picardie Jules Verne, CNRS-UMR 7314, F-80039 Amiens Cedex 1, France*

[2] *CNRS, Univ. Bordeaux, Bordeaux INP, ICMCB UMR 5026, F-33600 Pessac, France*

[3] *TIAMAT, 15 Rue Baudelocque, 80000 Amiens*

[4] *CELLS-ALBA Synchrotron, Cerdanyola del Vallès, E-08290 Barcelona, Spain*

[5] *RS2E, Réseau Français sur le Stockage Electrochimique de l'Energie, FR CNRS 3459, F-80039 Amiens Cedex 1, France*

Corresponding Authors

* laurence.croguennec@icmcb.cnrs.fr
* christian.masquelier@u-picardie.fr

Abstract

Vanadium multi redox reactions of $V^{4+/3+}$ and $V^{5+/4+}$ can contribute to significant capacity gain in positive electrodes for Na-Ion batteries, but the activation of $V^{5+/4+}$ redox couple is often accompanied by asymmetric and irreversible electrochemical reactions that are very important to understand for developing high capacity materials while maintaining the structural stability. Here, the asymmetric Na^+ extraction/insertion process in Fe/V-mixed NASICON $Na_4FeV(PO_4)_3$ electrode material is thoroughly investigated from both local and bulk perspectives. X-ray diffraction analysis demonstrates that the Na(1) site is depopulated at the third charge domain when the of $V^{5+/4+}$ redox couple is activated. Local environments of Fe and V were investigated through Mössbauer and X-ray absorption spectroscopies. The results point towards the existence of a distorted VO_6 octahedral environment, including a short V – O bond, when the $V^{5+/4+}$ redox couple is activated at high voltage. This study presents valuable aspects of the asymmetric behavior during multi-electron reactions that are commonly observed in V-based NASICON materials.

Introduction

Since the NASICON (Na-superionic-conductors) structure was initially proposed for fast Na^+ ionic transport by Hong and Goodenough in 1976[1], today it is studied as solid electrolytes, electrode materials as well as coating materials for different battery technologies (Li-ion, Na-ion and all-solid-state batteries) by tuning its composition.[2–8] In the late nineties, $Li_3M_2(PO_4)_3$ (M= V, Fe) NASICON compositions were for instance widely investigated as positive electrode materials for Li-ion batteries.[9–12] In more recent years, with the explosion of research activities within the Na-ion battery field, Na-rich NASICON-type electrode materials are back in the spotlight.[4–6,8]

It is well known that the NASICON structure of general formula $A_xMM'(XO_4)_3$ (A = Li, Na, X = P, S, Si) can lead to long electrochemical cycle life due to its robust 3D open framework. Nevertheless, up to now, its specific capacity was generally limited to 100-120 mAh/g with the exchange of 2 Na^+ ions per formula unit corresponding to that of 1 e^- per transition metal ion.[4–6,8,13] Therefore, the challenge is to improve the specific capacity of NASICON-type materials while maintaining their high structural stability.

One way to increase this specific capacity is to consider transition metals that can exchange more than 1 e^-. For instance, Mn and V can involve multi-electron reactions with the Mn^{4+}/Mn^{3+} and Mn^{3+}/Mn^{2+} redox couples for the first, and V^{5+}/V^{4+} and V^{4+}/V^{3+} for the second. Compositions were thus explored combining Mn at the divalent state with $Cr^{4+/3+}$ [14–16] or $Ti^{4+/3+}$ [17,18], as well as V at the trivalent state with $Mn^{3+/2+}$ [19,20] or $Fe^{3+/2+}$ [21–24]. In more recent years, mixing even more than two transition metals such as $VMn_{0.5}Fe_{0.5}$,[22] $V_{0.8}Al_{0.2}Mn$,[25] and $Fe_{0.4}Mn_{0.4}V_{0.4}Ti_{0.4}Cr_{0.4}$[26] was investigated attempting, similarly to strategies widely developed in layered oxides, to reach higher specific capacity and energy density while maintaining good capacity retention.

In the case of the mixed Fe/V system $Na_4Fe^{2+}V^{3+}(PO_4)_3$, three distinct voltage domains are identified in the charge process when extracting Na^+ from the structure

including the $V^{5+/4+}$ redox couple at high voltage. Only two domains are then observed during the subsequent discharge with the voltage-composition profile becoming more sloping.[21–24] The Fe/V-mixed NASICON compounds show relatively good electrochemical cycling stability maintaining this asymmetric electrochemical reaction in the following cycles.[21–24] The demonstration of the multi-electron reactions of vanadium in this system was already reported in several studies [21–24,27,28], while the reason for the asymmetric electrochemical reaction mechanism still remains not understood. Here we thus challenge the comprehension of the Na^+ extraction/insertion mechanism in $Na_4FeV(PO_4)_3$, including the V^{5+}/V^{4+} redox couple that is activated at high voltage, combining *operando* synchrotron X-ray powder diffraction to Mössbauer and X-ray absorption spectroscopies. These new insights obtained at both the long and local scales will give a detailed description of the local environments of iron and vanadium, at the origin of the electrochemical activity of $Na_4FeV(PO_4)_3$ and directly related to its asymmetry between charge and discharge.

Experimental

***Synthesis*:** $Na_4FeV(PO_4)_3$ was prepared by an electrochemical pre-sodiation method using $Na_3FeV(PO_4)_3$ as a precursor. To prepare $Na_3FeV(PO_4)_3$, stoichiometric amounts of Na_3PO_4 (Acros organics, 96 %), $FePO_4 \cdot 2H_2O$ (Sigma-Aldrich) and home-made VPO_4 in a molar ratio of 1:1:1 were ball-milled using a SPEX 8000 miller for 1 h. VPO_4 was synthesized by mixing of stoichiometric amount of V_2O_5 (Alfa Aesar, 99,6%), H_3PO_4 (Alfa Aesar, 85%), and agar-agar (Fisher BioReagents) in deionized water at 80 °C. The resulting powder was milled and annealed at 890 °C for 2 h in Ar. The resulting powder was heat-treated at 400 °C for 4 hours in Ar, and followed by annealing at 800 °C for 10 hours in Ar. Then, the obtained $Na_3FeV(PO_4)_3$ powder was electrochemically sodiated to form $Na_4FeV(PO_4)_3$ down to a cut-off voltage of 1.3 V vs. Na^+/Na, using Na metal counter electrode in a half-cell configuration. The electrolyte used for the pre-sodiation was composed of 1 M $NaPF_6$ in ethylene carbonate (EC) / dimethyl carbonate (DMC) (1:1, w/w) with 2 wt.% of fluoroethylene carbonate (FEC). More detailed synthesis descriptions can be found elsewhere.[24]

The morphology of the as-prepared $Na_3FeV(PO_4)_3$ powder was examined by scanning electron microscopy (SEM) with a Hitachi Model S-4500 microscope.

Electrochemical Measurements: Electrochemical tests were performed in CR2032-type coin cells with a half-cell configuration. The working electrode was comprised of the pre-sodiated $Na_4FeV(PO_4)_3$, carbon black (Alfa Aesar, 99.9+%), and polytetra-fluoroethylene (PTFE, Sigma-Aldrich, 99.9 %) as a binder with a ratio of 68/29/3 in wt.%. The mass loading of the active material in the electrode was 16.5 mg/cm^2. Na metal was used as a counter/reference electrode. The same electrolyte used in the pre-sodiation step was used for all the electrochemical tests. One sheet of each Whatman glass fiber (GF/D) and Celgard was used as a separator. The battery cell was cycled with a C-rate of C/15 (=15 h for the exchange of 1Na$^+$ / 1e$^-$) with a voltage window of 1.3 – 4.3 V vs. Na$^+$/Na.

Operando Synchrotron X-ray Diffraction: *Operando* synchrotron X-ray powder diffraction (XRPD) measurements were carried out on the MSPD beamline of the ALBA synchrotron in Spain[29] using Debye−Scherrer geometry with a wavelength of 0.8266 Å. The SXRPD patterns were recorded every ~30 minutes with an acquisition time of ~3.5 minutes in the 2θ angular range of 2–40°, with a 2θ step size of 0.006° using a MYTHEN detector. An *in situ* coin cell with two glass windows was used. The pre-sodiated $Na_4FeV(PO_4)_3$ electrode with the same formulation (68/29/3 in wt.%) was used with the mass loading of the active material of 17.3 mg/cm^2. One sheet of Whatman glass fiber (GF/D) was used as a separator. The *in situ* battery cell was cycled with a C-rate of C/15 in a voltage window of 1.0 – 4.3 V vs. Na$^+$/Na. Diffraction data analysis was performed using the FullProf Suite.[30] The evolution of the unit cell volume per formula unit (*V/Z*) was analyzed with a profile matching mode and several selected XRPD patterns were analyzed with the Rietveld method.

Mössbauer measurements: ^{57}Fe Mössbauer spectra were recorded using a constant acceleration Halder-type spectrometer in transmission geometry with ^{57}Co source at room temperature. Calibration of the velocity scale was done with a pure α-Fe^0 foil as reference. Mössbauer parameters including isomer shift (δ), quadrupole

splitting (Δ), full-width at half-maximum (Γ) and relative area (%) were refined using the WinNormos software (Wissenschaftliche Elektronik GmbH).

***X-ray absorption spectroscopy* (XAS)**: XAS measurements were performed in transmission mode at the ROCK beamline of the SOLEIL synchrotron in France.[31] A Si(111) quick-XAS monochromator was used with an oscillation frequency of 2 Hz at the Iron and Vanadium K-edges. Three ionization chambers were used as detectors and the energy calibration was ensured by placing Fe or V foils between the second and the third ionization chamber. The Fe and V XAS spectra were recorded on the same ex situ sample by averaging over 10 minutes of acquisition time. The analyses were performed with Athena and Artemis from the Demeter software package.[32] The oxidation state of Fe and V was inferred by the edge position taken at normalized absorption of 1. The detailed procedures of the data analysis were described in our previous work.[24]

Results and Discussion

As reported in our previous work[24], the pre-sodiated $Na_4FeV(PO_4)_3$ compound recovered at 1.3 V vs. Na^+/Na crystallizes in a structure described in the *R*-3*c* space group, and no impurities such as $NaFePO_4$ and Na_3PO_4 were detected based on XRD analysis (**Figure S1**). The refined cell parameters using the Rietveld method are a = 8.94656(8) Å, c = 21.3054(3) Å, V/Z = 246.140(4) Å^3, and occupancy factors for the Na(1) and Na(2) sites are 0.958(5) and 0.958(8) respectively, resulting in the $Na_{3.83(3)}FeV(PO_4)_3$ global composition.

SEM images of the as-prepared $Na_3FeV(PO_4)_3$ powder (**Figure S2**) show that most of the particles' sizes are in the range of several hundred nanometers to few microns, but rather large agglomerates (> 20 µm) were also found. Optimization of the particle size was out of the scope in this study, although particle size distribution of the active material can influence the electrochemical performance.

Electrochemical voltage profiles of the as-prepared $Na_3FeV(PO_4)_3$ within two voltage windows of 2-3.75 V (vs. Na^+/Na) and 2-4.3 V and of the pre-sodiated $Na_4FeV(PO_4)_3$

within the voltage window of 1.3-4.3 V are compared in **Figure S3**. The voltage profiles ascribed to the $V^{4+/3+}$ and $V^{5+/4+}$ redox couples of the as-prepared $Na_3FeV(PO_4)_3$ are shown to be very similar to those observed for the pre-sodiated $Na_4FeV(PO_4)_3$, although the former compound does not show the redox activity of $Fe^{3+/2+}$. As can be seen from the comparison of the two voltage windows of 2-3.75 V and 2-4.3 V, the voltage profile of the as-prepared $Na_3FeV(PO_4)_3$ becomes sloping once $V^{5+/4+}$ redox couple is activated.
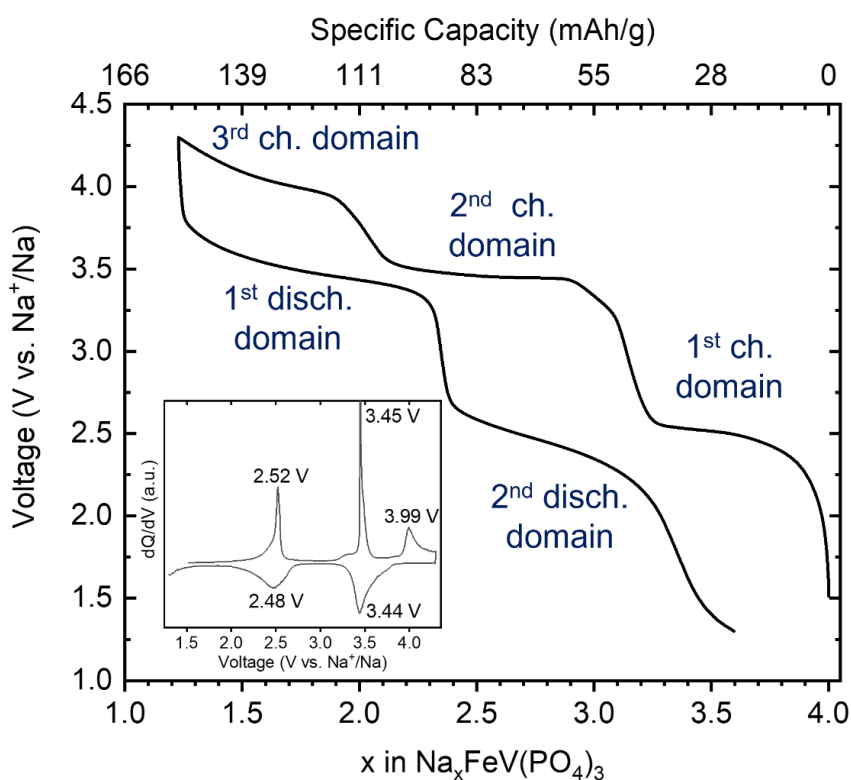

Figure 1. Electrochemical charge and discharge curves obtained for the pre-sodiated $Na_4FeV(PO_4)_3$ electrode material when cycled in a half cell versus Na metal between 1.3 - 4.3 V with a C-rate of C/15 (1 Na^+ in 15 h).

To investigate the mechanism of the asymmetric electrochemical reaction occurring during charge and discharge, galvanostatic charge-discharge data of $Na_4FeV(PO_4)_3$ were recorded between 1.3 V and 4.3 V with the C-rate of C/15 (= 1 Na^+ exchanged in 15 hours). Voltage profile versus composition during the first cycle, and the corresponding derivative (dQ/dV) plot are presented in **Figure 1**. During charge, three voltage domains are observed at around 2.52 V, 3.45 V, and 3.99 V. Note that

the second domain can be divided into three sub-domains: It starts with a small solid-solution subdomain then followed by a voltage plateau, and then by a rather sloping curve again. This can also be seen in the corresponding derivative curve (inset of **Figure 1**), and in the voltage profile of quasi-galvanostatic intermittent titration technique (GITT) as shown in **Figure S4** During discharge, however, only two main domains are found with the average voltages of 3.44 V and 2.48 V, with all over the composition range a more sloping voltage curve.
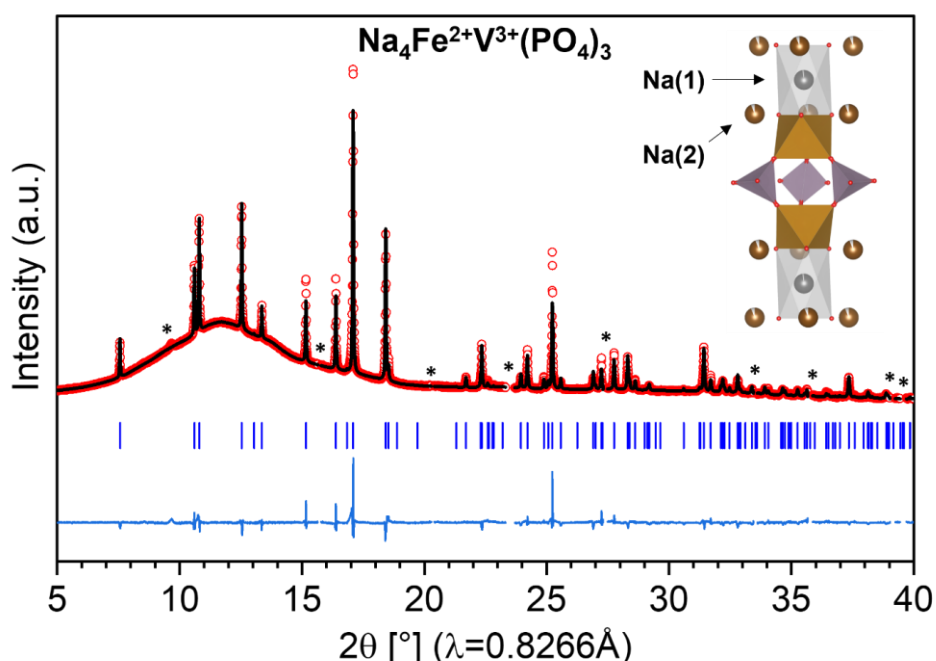

Figure 2. Rietveld refinement profile obtained for $Na_4FeV(PO_4)_3$, from the synchrotron XRPD pattern collected with the *in situ* cell before cycling. The asterisk marks indicate the reflection peaks associated to PTFE, Na metal and Al foil (see the details in **Figure S3**). Refined structural parameters is listed in **Table S1**.

A series of synchrotron XRPD patterns were collected *operando* during the electrochemical cycling of $Na_4FeV(PO_4)_3$ vs. Na metal to investigate the structural evolution associated with each electrochemical signature observed during Na^+ extraction/insertion from $Na_4VFe(PO_4)_3$. **Figure 2** shows the XRPD pattern of $Na_4FeV(PO_4)_3$ collected in the *in situ* cell before electrochemical operation. The excluded regions indicated by asterisk marks originate from the Na metal and the Al foil, and they were not considered during the refinement (see **Figure S5** for

comparison with the full XRPD pattern without these excluded regions). The refined cell parameters are $a = 8.94160(9)$ Å, $c = 21.3148(4)$ Å and $V/Z = 245.974(5)$ Å^3. The refined sodium occupancy factors for Na(1) and Na(2) sites are 0.98(4) and 0.938(15), respectively, resulting in the $Na_{3.79(9)}FeV(PO_4)_3$ composition. Compared to the structural parameters and composition determined for $Na_4FeV(PO_4)_3$ from the Rietveld refinement of the XRPD pattern collected within a capillary, just after its synthesis, smaller unit cell volume (245.974(5) Å^3 vs. 246.140(4) Å^3) and Na content (3.79(9) vs. 3.83(3)) are determined for the same powder within the *in situ* cell just before cycling, suggesting a slight self-charge. Note that the pre-sodiation process to prepare $Na_4FeV(PO_4)_3$ was performed 3 days prior to collecting data at the ALBA synchrotron. The comparison of the electrochemical charge and discharge curves obtained for $Na_4FeV(PO_4)_3$ vs. Na metal in a normal coin cell and in the *in situ* cell shows an overall good agreement but also reveals that about 0.1 less Na$^+$ is involved in the first charge domain obtained in the *in situ* cell (**Figure S6**).
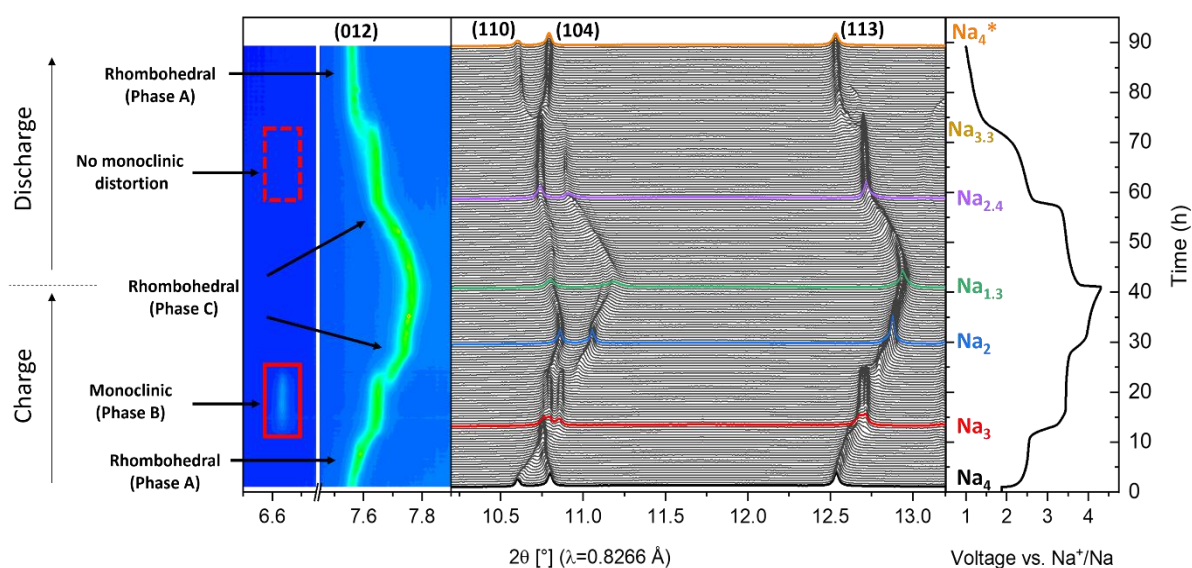
Figure 3. *S*ynchrotron XRPD patterns collected *operando* during the first cycle of $Na_4FeV(PO_4)_3$ vs. Na metal within a voltage window of 1.0 - 4.3 V at a C-rate of C/15 (1 Na$^+$ in 15 h). * Composition estimated from the Rietveld refinement of the XRPD pattern (see the text for details).

Figure 3 displays the synchrotron XRPD patterns collected *operando* during the first cycle of the battery within the voltage window of 1.0 – 4.3 V vs. Na$^+$/Na at a C-rate of C/15 (for a wider 2θ range (5-30° (2θ)), see **Figure S7)**. The associated unit cell

volume evolution is shown in **Figure 4**. Refined cell parameters, V/Z, and occupancies of the two Na(1) and Na(2) sites are summarized in **Table 1** for selected compositions obtained in charge and discharge. $Na_xFeV(PO_4)_3$ electrode material undergoes a complex Na^+ extraction/insertion mechanism with a succession of solid-solution and two-phase reactions during cycling. During the first charge domain up to 2.6 V, around 0.8 Na^+ is extracted through a solid-solution reaction since the Bragg peaks continuously shift from those observed for the single pristine $Na_4FeV(PO_4)_3$ phase. The corresponding unit cell volume per formula unit (V/Z) decreases by 2.3 % from 245.974(5) $Å^3$ to 240.282(17) $Å^3$ (**Figure 4**)

Coming close to the composition of $Na_3FeV(PO_4)_3$, the structure undergoes a monoclinic distortion, specifically spotted by the existence of the Bragg peak at around 6.6° (d = 6.13 Å, see the full 2θ range in **Figure S8**). A V/Z value contraction of 0.9 % from 240.282(17) $Å^3$ to 238.208(11) $Å^3$ is observed when this phase transformation occurs, requiring the description of the unit cell in the *C*2/*c* space group in order to take into account all the superstructure reflections highlighted in **Figure S8**. This supercell indicates a Na^+/vacancy ordering[24] as commonly spotted in other $Na_3MM'(PO_4)_3$ compositions ($Na_3Fe_2(PO_4)_3$,[33] $Na_3V_2(PO_4)_3$,[34] $Na_3VTi(PO_4)_3$,[35] $Na_3Ti_2(PO_4)_3$[36]). From $Na_3FeV(PO_4)_3$ (Phase B) to $Na_2FeV(PO_4)_3$ (Phase C) between 3.4 V and 3.75 V, there are three sub-domains (labeled as region I, II, and III) in the second charge domain, where the corresponding electrochemical mechanism occurs through a successive mechanism of monophasic – biphasic – monophasic reactions (**Figure 4**). The details of the corresponding synchrotron XRPD patterns for regions I, II, and III are presented in **Figure 4b**. In region I, phase B evolves according to a solid-solution as shown by the trivial peak shift between scan # 23 and scan 38, then a two-phase reaction between phase B and a new phase C described in the *R*-3*c* space group and characterized by the composition $Na_{2.5}FeV(PO_4)_3$ (region II, scan # 38—50) is observed, followed finally by a solid-solution reaction until the composition $Na_2FeV(PO_4)_3$ (region III, scan # 50 – 58). It is noticed that the region (II) where the two phases coexist is narrow, and this was also observed in other studies for $Na_xFeV(PO_4)_3$ [23] and $Na_xMnCr(PO_4)_3$[15].
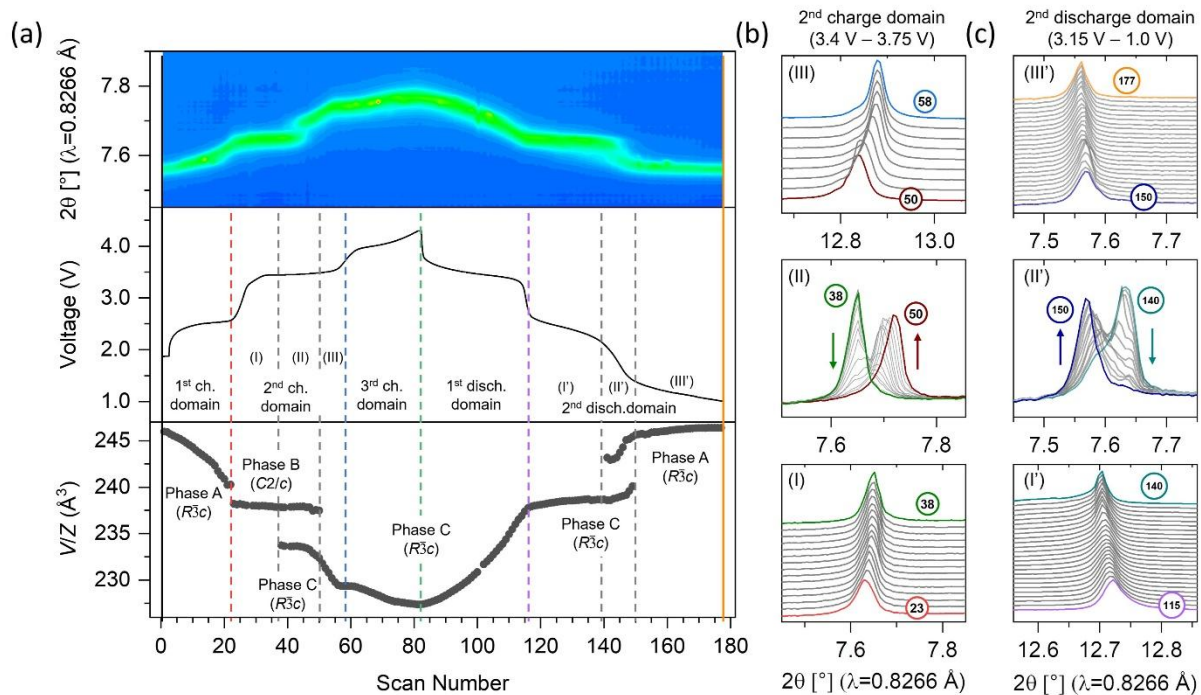
Figure 4. (a) The evolution of the unit cell volume per formula unit (*V/Z*) (bottom), obtained from the full pattern matching refinement of the synchrotron XRPD patterns collected operando during the cycling of the *in situ* cell, is associated to the electrochemical curve (middle) and to the evolution in 2θ of the (012) diffraction line (top). **(b)** Enlarged view of the synchrotron XRPD patterns during the three sub-domains (regions I, II, and III) on the second charge domain (3.4 V – 3.75 V) and **(c)** Enlarged view of the synchrotron XRPD patterns during the three sub-domains (regions I', II', and III') on the second discharge domain (3.15 V – 1.0 V)

From $Na_2FeV(PO_4)_3$ to $Na_{1.3}FeV(PO_4)_3$, in the third charge domain between 3.75 V and the end of charge at 4.3 V, around 0.8 Na^+ is further extracted through a solid-solution reaction. The Na(1) site, that remained almost fully filled until that extraction ratio, starts to depopulate in this voltage domain with an occupancy ratio evolving from 0.98(4) to 0.71(6). In fact, from the composition $Na_2FeV(PO_4)_3$ (*i.e.* as soon as the third domain is reached) Na^+ ions are extracted from both Na(1) and Na(2) sites, making Na^+ distribution within the structure much more disordered. As the Na^+ ions in Na(1) site are placed along the $[001]_{Hexagonal}$ direction, a depopulation of Na(1) site leads to an increase in c parameter from 21.58893(4) to 21.9030(14) Å due to an increasing repulsion between the oxygen atoms along the same direction.[10,11,37]

11

For the overall charge process, the cell volume (V/Z) decreases by 7.3 % from 245.974(5) to 227.897(5) Å^3 (**Figure 4**). When this value is compared with the extraction of ~3 Na^+ in other NASICON compounds, it appears comparable with that observed for the Mn/Cr system ($\Delta V/V$= -7.7 % when charged up to 4.7 V[16]) and smaller than that observed for the Mn/V system ($\Delta V/V$= -9.3 % when charged up to 4.0 V[19] and $\Delta V/V$= -10.1 % when charged up to 4.3 V[20]).

After charging the battery up to 4.3 V, the voltage profile of the discharge is different from that of the charge. During the first discharge domain from 4.3 V to 3.15 V, about 1.1 Na^+ ions are re-intercalated in $Na_{1.3}FeV(PO_4)_3$ through a solid-solution mechanism with the increase of the unit cell volume (V/Z) from 227.897(5) to 237.358(5) Å^3.

The second part of the discharge process from 3.15 V until the end of discharge at 1.0 V can also be divided into three sub-domains (labeled as region I', II', and III') with an electrochemical mechanism of monophasic – biphasic – monophasic reactions (see the details in **Figure 4a and 4c**). A unit cell volume evolves from 237.358(5) to 246.378(5) Å^3 and reaches the composition $Na_{3.84(9)}FeV(PO_4)_3$, which is very close to that of the pristine pre-sodiated $Na_4FeV(PO_4)_3$ compound. This material recovered after the first charge and discharge cycle appears in fact slightly more sodiated compared to the pristine compound before the *operando* XRD measurement, with a different distribution of the Na^+ ions among the Na(1) and Na(2) sites. The occupancy of the Na(1) site evolves from 0.98(4) (almost full) in the pristine state, towards 0.71(6) at 4.3 V showing its clear depopulation in the charge state of the battery. It comes back to 0.89(4) at the end of the discharge: these remaining vacancies on the Na(1) sites would be at the origin of a disorder that prevents any Na^+/vacancy ordering and thus the monoclinic distortion to occur for about $Na_3FeV(PO_4)_3$ composition.

Note that the side reaction that originates from the conductive carbon additive in contact with the electrolyte[24,38] contributes to the electrochemical reaction below 1.5 V (mainly in region III'), concomitantly with Na^+ insertion in the active material $Na_xFeV(PO_4)_3$. Therefore, the value of x = ~4.5 (**Figure S6**) reached at the end of

discharge and calculated from the number of electrons exchanged during the electrochemical reaction shows a significant mismatch with the actual x value in $Na_xFeV(PO_4)_3$ (here 3.84(9)) determined from the Rietveld refinement, as this side reaction was not considered. To avoid any confusion, the x value given in **Figure 3** at the end of discharge is determined from the Rietveld refinement only and shown to be close to Na_4 instead of $Na_{4.5}$ as declared by the electrochemical reaction.

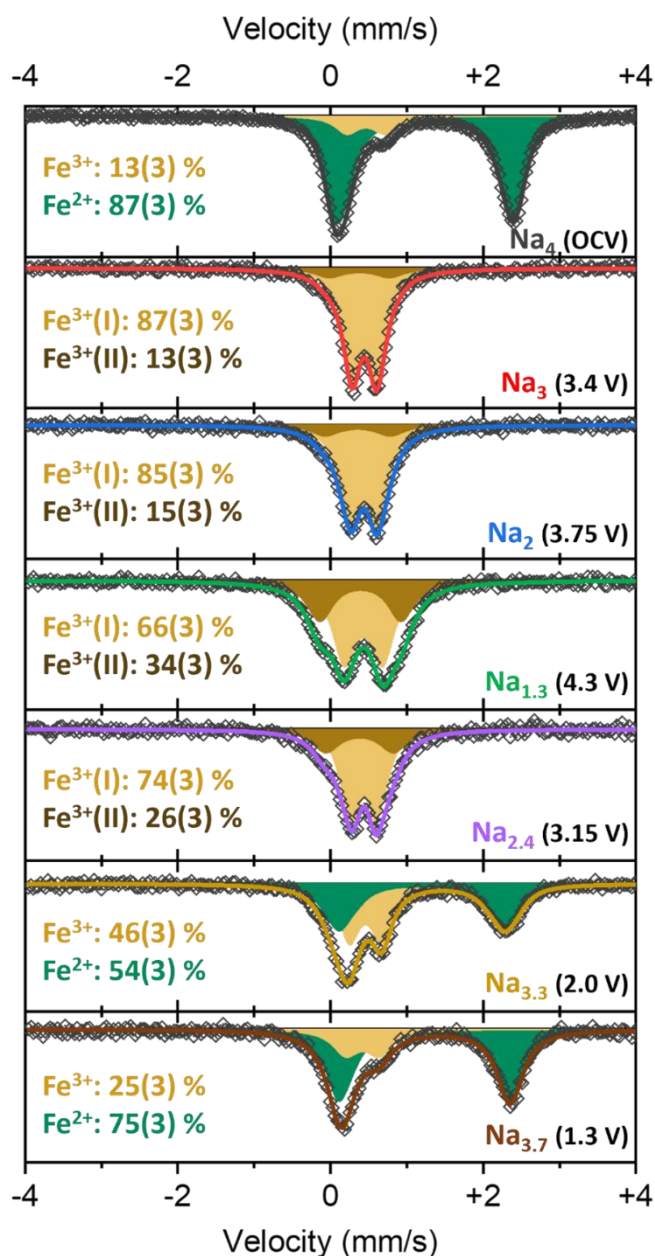**Figure 5.** Room temperature ^{57}Fe Mössbauer spectra collected *ex situ* for $Na_xFeV(PO_4)_3$ recovered at various states of charge and discharge. The quadrupole doublets that describe

the spectra are associated with Fe^{2+} (green), Fe^{3+}(I) (light brown), and Fe^{3+}(II) (dark brown). The corresponding refined hyperfine parameters are summarized in **Table S6**.

Table 1. Space group (S.G.), unit cell parameters, V/Z value and Na site occupancy factors determined from the Rietveld refinement of synchrotron XRPD patterns collected *operando* at different states of charge and discharge of the battery. The total Na content per formula unit is determined from the Na site occupancy factors. The detailed results of the Rietveld refinements are summarized in **Tables S1-S5** and **Figures S9-S11**. *The cell parameters were refined with a profile matching and the Na occupancy factors were taken from ref. [24].

	Voltage	S.G.	a (Å)	b (Å)	c (Å)	β (°)	V/Z (Å^3)	Na(1) Occ.	Na(2) Occ.	Total Na /f.u.
$Na_4FeV(PO_4)_3$	OCV	*R-3c*	8.94160(9)	8.94160(9)	21.3148(4)	120	245.974(5)	0.98(4)	0.938(15)	3.79(9)
***$Na_3FeV(PO_4)_3$**	3.4 V	*C2/c*	15.1445(2)	8.72473(11)	21.6115(3)	90.1924(8)	237.962(6)	1	0.67	3
$Na_2FeV(PO_4)_3$	3.75 V	*R-3c*	8.57794(11)	8.57794(11)	21.58893(4)	120	229.286(6)	0.98(4)	0.416(16)	2.23(9)
$Na_{1.3}FeV(PO_4)_3$	4.3 V	*R-3c*	8.4904(3)	8.4904(3)	21.9030(14)	120	227.897(5)	0.71(6)	0.20(3)	1.31(8)
$Na_{2.4}FeV(PO_4)_3$	3.15 V	*R-3c*	8.6819(3)	8.6819(3)	21.8170(10)	120	237.358(5)	0.91(5)	0.54(2)	2.54(12)
$Na_{4.5}FeV(PO_4)_3$	1.0 V	*R-3c*	8.94445(10)	8.94445(10)	21.3364(4)	120	246.382(5)	0.89(4)	0.984(16)	3.84(9)

To investigate changes in the oxidation state and local environment of iron during electrochemical cycling, *ex situ* ^{57}Fe Mössbauer spectroscopy experiments were performed at room temperature using air-tight sample holders prepared under argon atmosphere. **Figure 5** shows the Mössbauer spectra collected for a series of key compositions $Na_xFeV(PO_4)_3$ obtained at different states of charge or discharge during the first cycle.

Each Mössbauer spectrum may be considered as the sum of two components (quadrupole doublets) whose refined hyperfine parameters are summarized in **Table S6**. They correspond to typical high-spin Fe^{2+} or Fe^{3+} in octahedral environments with oxygen ligands.[21,24,39,40] During the first domain of charge process, Fe^{2+} is fully oxidized to Fe^{3+} associated with the extraction of the first Na^+. After that, until the end of charge at 4.3 V, no further oxidation of Fe is observed, but two Fe^{3+} environments are identified, labeled as Fe^{3+}(I) and Fe^{3+}(II).

At 4.3 V, the two environments display minor differences in isomer shift values of 0.43(1) and 0.39(2) mm/s for Fe^{3+}(I) and Fe^{3+}(II), respectively, but a significant

14

difference in quadrupole splitting value of 0.51(3) and 1.08(5) mm/s for $Fe^{3+}(I)$ and $Fe^{3+}(II)$, respectively. As a more anisotropic iron octahedral environment tends to have lower isomer shifts[39], which are also influenced by the degree of Fe – O bond covalence or ionicity, $Fe^{3+}(II)$ can be a slightly more distorted environment than $Fe^{3+}(I)$. Note that a different distribution of the first cationic neighbors (i.e. V^{4+}, V^{5+}, or Fe^{3+} at 4.3 V) or the presence of a distorted VO_6 environment in the lantern VO_6-$(PO_4)_3$-FeO_6 can generate a more disordered/distorted Fe environment responsible for higher values of the quadrupole splitting parameter, which strongly depends on the electric field gradient produced by the ligands and the first cationic neighbours at the iron nucleus.
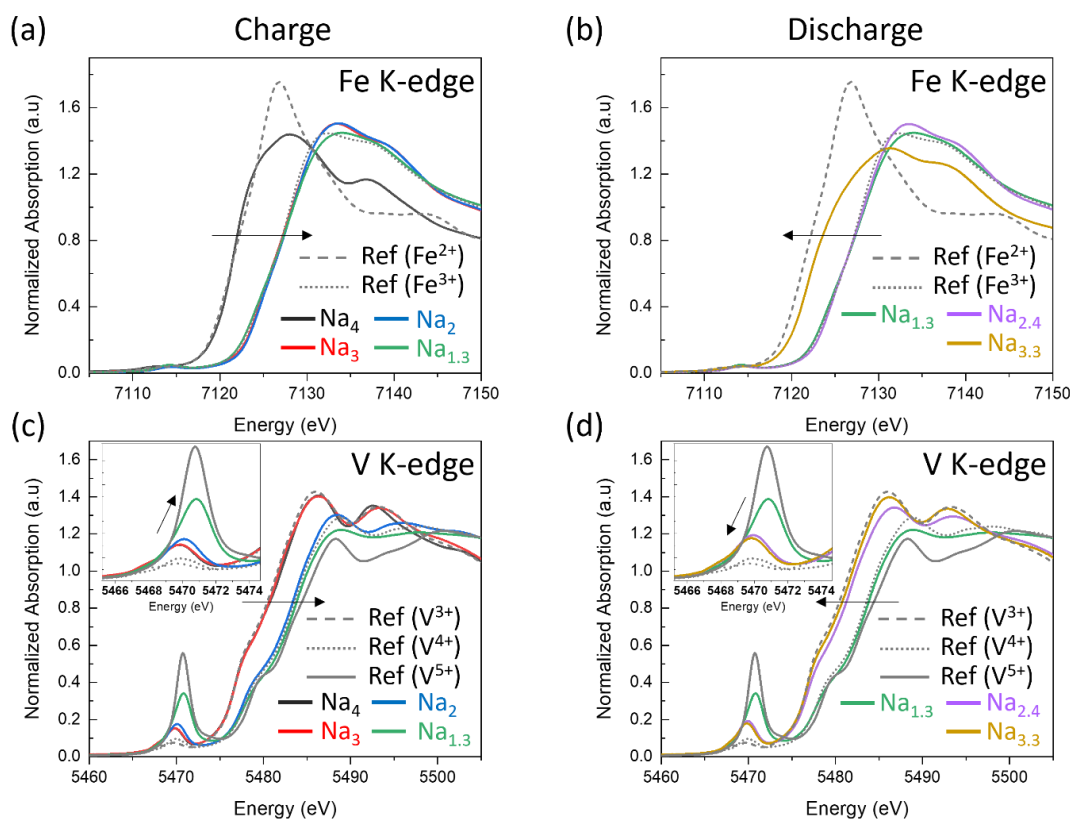
Figure 6. XANES spectra collected on *ex situ* $Na_xFeV(PO_4)_3$ compounds recovered at different states of charge or discharge of the battery. Spectra obtained at the Fe K-edge during (a) charge and (b) discharge. V K-edge spectra obtained during (c) charge and (d) discharge. References for Fe and V K-edge XAS spectra: Fe^{2+} ($FeC_2O_4 \cdot 2H_2O$), Fe^{3+} ($Na_3Fe_2(PO_4)_3$), V^{3+} ($Na_3V_2(PO_4)_3$), V^{4+}($Na_1V_2(PO_4)_3$) and V^{5+}($VOPO_4$).

These isomer shift and quadrupole splitting values are in good agreement with those previously reported by Mortemard de Boisse et al. in their study of $Na_{3.5-x}Fe_{0.5}V_{1.5}(PO_4)_3$ at different states of charge.[21] Moreover, the proportion of distorted Fe local environment, $Fe^{3+}(II)$, increases continuously upon further Na^+ extraction until 34(3)% at the end of charge. In the following discharge process, this proportion decreases to 26(3) % at 3.15 V, before disappearing at 2.0 V. This suggests that the changes in the local environment of Fe are reversible, despite about 25(3) % of iron remaining unreduced as $Fe^{3+}(I)$ at the end of discharge at 1.3 V.

To further investigate changes in the local environment and oxidation state of iron and vanadium, X-ray spectroscopy experiments were performed on *ex situ* samples. X-ray Absorption Near-Edge Structure (XANES) spectra collected at the Fe and V K-edges for a series of $Na_xFeV(PO_4)_3$ compounds recovered at different states of charge or discharge during the first cycle are compared in **Figure 6.**

XANES results confirm that Fe^{2+} is oxidized to Fe^{3+} (**Figure 6a**) while V^{3+} remains unchanged (**Figure 6c**) during the first charge domain. After that, the oxidation state of iron does not change anymore until the end of the charge process, even if the shape of the spectra is modified (**Figure 6a**), implying the modification of the local environment around Fe^{3+} as revealed also by Mössbauer spectroscopy. During discharge, Fe^{3+} is reduced to Fe^{2+} only from the beginning of the second discharge domain, from 3.15 V and until 2.0 V (**Figure 6b**). At 2.0 V, Fe is partly oxidized as the edge energy of 7124.9 eV is intermediate between that of 7122.6 eV for Fe^{2+} and that of 7128.3 eV for Fe^{3+}. Therefore, only 60% of iron would be at the divalent state at 2.0 V from XANES analysis, in good agreement with the 54 % determined from the Mössbauer data. Nevertheless, from Mössbauer spectroscopy it was also shown that further reduction of iron can proceed at lower voltage than 2.0 V.

At the V K-edge, during the second charge domain, the edge energy increases from 5481.9 to 5484.5 eV indicating the oxidation of V^{3+} to V^{4+} (**Figure 6c**). In the third charge domain, vanadium is oxidized further as shown by the shift of the edge from 5484.5 to 5485.1 eV. In parallel, the intensity of the pre-edge increases drastically by a factor of ~2 with a shift in energy from 5470.0 to 5470.8 eV, which is characteristic

of V^{5+}.[41–45] This increasing intensity of the pre-edge also indicates a higher degree of distortion for the V environment, as also observed in other V-based NASICON compounds when the V^{5+}/V^{4+} redox couple is activated.[41–45]

During discharge, as shown in **Figure 6d**, V^{4+} and $V^{5+·}$ are reduced towards V^{3+} during the first domain ($Na_{2.4}$) and fully reduced to V^{3+} at 2.0 V ($Na_{3.3}$). Indeed, the intensity of the pre-edge for the spectrum recorded at the end of charge (4.3 V) becomes much less intense for the spectrum recorded on $Na_{3.3}$ composition. Moreover, the edge position was shifted back to lower energy and very close to that of pristine material (**Figure S13**). This result reveals enhanced reversibility of the atomic and electronic changes occurring at the V site in $Na_4FeV(PO_4)_3$, whereas for other V-based NASICON compounds such as in the Mn/V system, once the V^{5+}/V^{4+} redox couple is activated, the environment of V remains highly distorted at the end of discharge of 2.75 V or 2.5 V.[41–43]

Based on these XANES analyses performed at the Fe and V K-edges, it can be concluded that the three voltage domains observed at 2.5 V, 3.45 V and 4.0 V upon charge can be assigned to the Fe^{3+}/Fe^{2+}, V^{4+}/V^{3+} and V^{5+}/V^{4+} redox couples, respectively, whereas the two voltage domains at 3.44 V and 2.5 V observed upon discharge correspond to mainly $V^{5+}/V^{4+}/V^{3+}$ and Fe^{3+}/Fe^{2+} respectively.

The amount of Na^+ exchanged through the activation of the $V^{4+/3+}$ and $V^{5+/4+}$ redox couples was about 1.8 during charge, however, only about 1.1 Na^+ was re-intercalated during the discharge process. Such behavior was also observed for other V-based NASICON materials as soon as the $V^{5+/4+}$ redox couple was activated.[21,23,24,44–46] It is interesting to point out that according to the study of $Na_3CrV(PO_4)_3$ by Liu et al.[44] when charged up to 4.3 V and then discharged down to the very low voltage of 1.4 V, the capacity unrecovered in discharge in the potential window expected for the activation of $V^{4+/3+}$ and $V^{5+/4+}$ redox couples appears to be partially retrieved only once the voltage is below 1.7 V. This may contribute during second discharge domain, apart from the contribution of possible side reactions at low voltage.

The Extended X-ray Absorption Fine Structure (EXAFS) analysis was performed to get more quantitative insight into the local environments of Fe and V. **Figure 7** illustrates the detailed Fe – O and V – O distances in the first coordination shells of Fe and V in $Na_xFeV(PO_4)_3$ compounds recovered at different states of charge or discharge of the battery. The magnitude of the k^2-weighted Fourier-transformed EXAFS oscillations and the corresponding backward Fourier transformed q-space are given in **Figures S14-S15**. We have only considered the first shell coordination of V and Fe, where the cation is surrounded by 6 oxygen atoms. The details about the fitting procedure are reported in the supplementary information. The refined EXAFS parameters are summarized in **Tables S7-S8**.
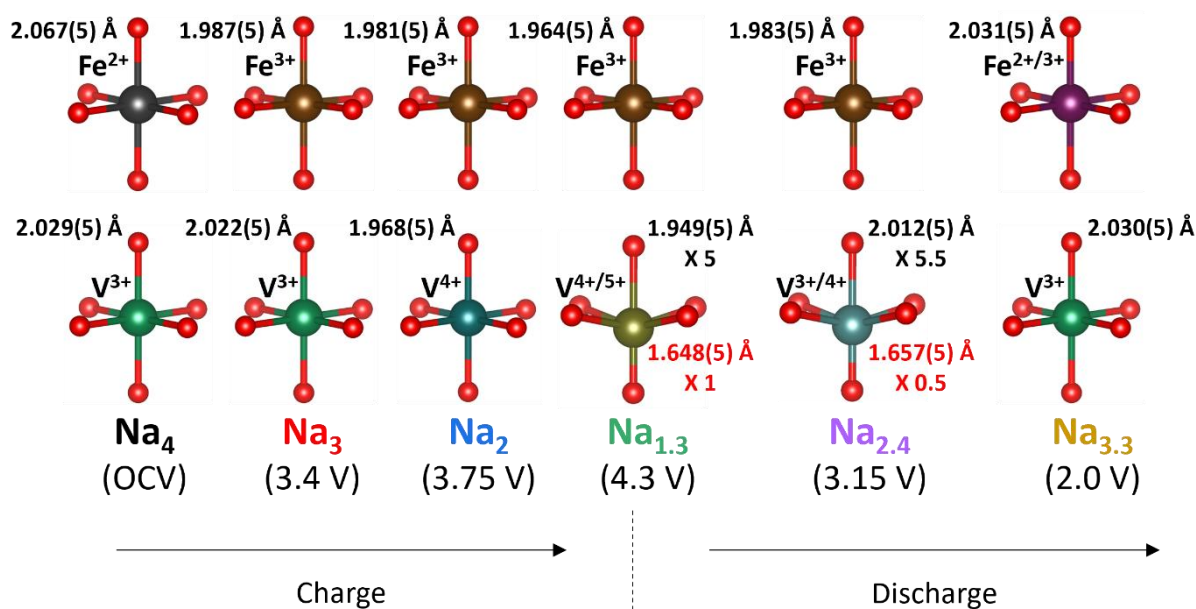

Figure 7. Iron and vanadium local environments in the first shells determined by EXAFS analysis from spectra collected for $Na_xFeV(PO_4)_3$ compounds recovered at different states of charge or discharge.

Only a single Fe-O distance was required, and thus used, for the refinements of the first coordination shell for all spectra, even at the end of charge, while Mössbauer spectroscopy shows two Fe^{3+} signals. The reason for this apparent discrepancy is that EXAFS gives an average local description of the probed element, and is thus much less sensitive than Mössbauer spectroscopy to distribution of oxidation states and local environments for Fe. Indeed, as mentioned before, the isomer shift, the

18

quadrupolar splitting and the line width are sensitive to the electronic and atomic structure around the probed nuclei. Nevertheless, the EXAFS results are in good agreement with those obtained by Mössbauer spectroscopy and allow quantifying changes in the Fe – O bond length all along with the Na^+ extraction/insertion reactions. The Fe - O bond length noticeably decreases from 2.067(5) to 1.987(5) Å during the first charge domain when Fe^{2+} ions are oxidized to Fe^{3+}. Then, this average bond length remains almost unchanged in the second charge domain (i.e. decreasing from 1.987(5) Å to 1.981(5) Å), before a slight contraction until 1.964(5) Å at the end of charge. This contraction in voltage domains where Fe itself is not involved in the redox processes highlights that the oxidation to V^{4+} and then until V^{5+} impacts the Fe environment. Upon discharge, the Fe - O bond length increases back to 2.031(5) Å, slightly smaller than that observed in the pristine material, in good agreement with the uncomplete reduction of Fe^{3+} to Fe^{2+} in the compound discharged down to 2.0 V.

Considering the V local environment, the first coordination shell is described by an isotropic VO_6 octahedral environment with 6 equivalent V - O bond lengths, nearly unchanged during the first charge domain (i.e. as shown by the slight decrease from 2.029(5) Å until to 2.022(5) Å) and then drastically shortened from 2.022(5) to 1.968(5) Å during the second charge domain when V^{3+} is oxidized to V^{4+}. At the end of charge at 4.3 V, however, a significant distortion was expected in the VO_6 octahedron as revealed by the appearance of intense pre-peak in the XANES region. Therefore, the [5+1] coordination model to describe the V local environment was made with five regular bonds of 1.938(5) Å and a short bond of 1.637(5) Å (**Figure 7**). Note that the [4+1+1] coordination model (equatorial-long-short bonds) was also attempted to fit the EXAFS data, resulting in the bond lengths of 1.938(5), 2.519(5), and 1.637(5) Å, respectively (**Table S9**). We concluded that the [5+1] model is more accurate than the [4+1+1] model as the R-factor allows one to define the accuracy/appropriateness of the model. Moreover, the probability of having such a relatively long bond in [4+1+1] model is low,[47,48] and a contribution of the second shell (V – P or V – Na) cannot be completely excluded in the R-range where the long bond can be possibly found. Nevertheless, note that the main message here is that a

short bond is absolutely required to describe VO_6 octahedron, while an isotropic [6] model leads to a drastic mismatch with the experimental data (**Figure S16**).

During the first discharge domain from 4.3 V to 3.15 V, the VO_6 environment becomes more symmetric but the short V – O bond partially remains. For these reasons, we have proposed a model including 5.5 oxygen atoms with a distance of 2.012(5) Å and 0.5 oxygen atoms with 1.657(5) Å, which can adequately describe the VO_6 octahedral environment for the EXAFS data recorded at 3.15 V for $Na_{2.4}Fe^{3+}V^{3+,4+}(PO_4)_3$ composition (see the details in **Figure S17** and **Table S10**). This VO_6 environment is in fact an average description combining symmetric and more distorted environments for V^{3+} and V^{4+}, respectively. The regular V - O bond distance of 2.012(5) Å is as expected between that of 2.022(5) Å for V^{3+} and that of 1.968(5) Å for V^{4+}. In the following discharge process occurring from 3.15 V to 2.0 V, the short V - O bond disappears and the VO_6 environment is back to isotropic again with V - O bond length of 2.030(5) Å, which is very close to that observed for the pristine materiel, before cycling. The EXAFS oscillations observed before and after the first cycling are globally maintained (**Figure S13**), implying relatively good reversibility of the process even if the local structure was strongly distorted at high voltage.

The results obtained from XRD, Mössbauer, and XAS are combined to explain the electrochemical reaction mechanism and the evolution of Fe and V local environments in the mixed Fe/V NASICON compound $Na_4FeV(PO_4)_3$ upon Na^+ extraction and then reinsertion, as shown in **Figure 8**. The first Na^+ removal proceeds through a solid-solution mechanism. Then, the $Na_3FeV(PO_4)_3$ composition obtained by the de-intercalation of 1 Na^+ per formula unit from $Na_4FeV(PO_4)_3$ undergoes Na^+/vacancy ordering. The extraction of the second Na^+ involves a two-phase reaction, preceded and followed by a solid solution mechanism. During the first two Na^+ extractions, Fe^{2+} is hence oxidized to Fe^{3+} first to 3.4 V, followed by the oxidation of V^{3+} to V^{4+} between 3.4 and 3.75 V. These two Na^+ are mostly electrochemically extracted from the Na(2) site while the Na(1) site remains almost fully occupied. Local environments of Fe and V are found to be symmetric and Fe – O and V – O distances decrease according to the order of the redox centers

activated for each voltage domain (main decrease in Fe – O bond length first followed then by that of V – O).

During the extraction of the third Na^+ ion, however, the Na(1) site begins to be depopulated and distorted Fe and V local environments are observed, including the distorted $V^{5+}O_6$ octahedral environment including vanadyl-like V – O short bond. These much-distorted Fe and V environments with a disorder on the Na sites induce an asymmetric electrochemical reaction mechanism in the subsequent discharge. The phase obtained at the end of the charge is re-intercalated according to a solid-solution mechanism during the first discharge domain, involving the concomitant $V^{5+/4+/3+}$ redox couples. In the lower voltage domain Na^+ is intercalated through a two-phase reaction, Fe^{3+} is reduced back to Fe^{2+}, and the distorted environments disappear, recovering symmetric surroundings for both Fe and V. However, charging at high voltage, having the deep sodiated phase at the end of charge, makes the reduction of Fe^{3+} to Fe^{2+} sluggish, hindering the complete reduction of iron, eventually resulting in a capacity loss upon cycling.[24]
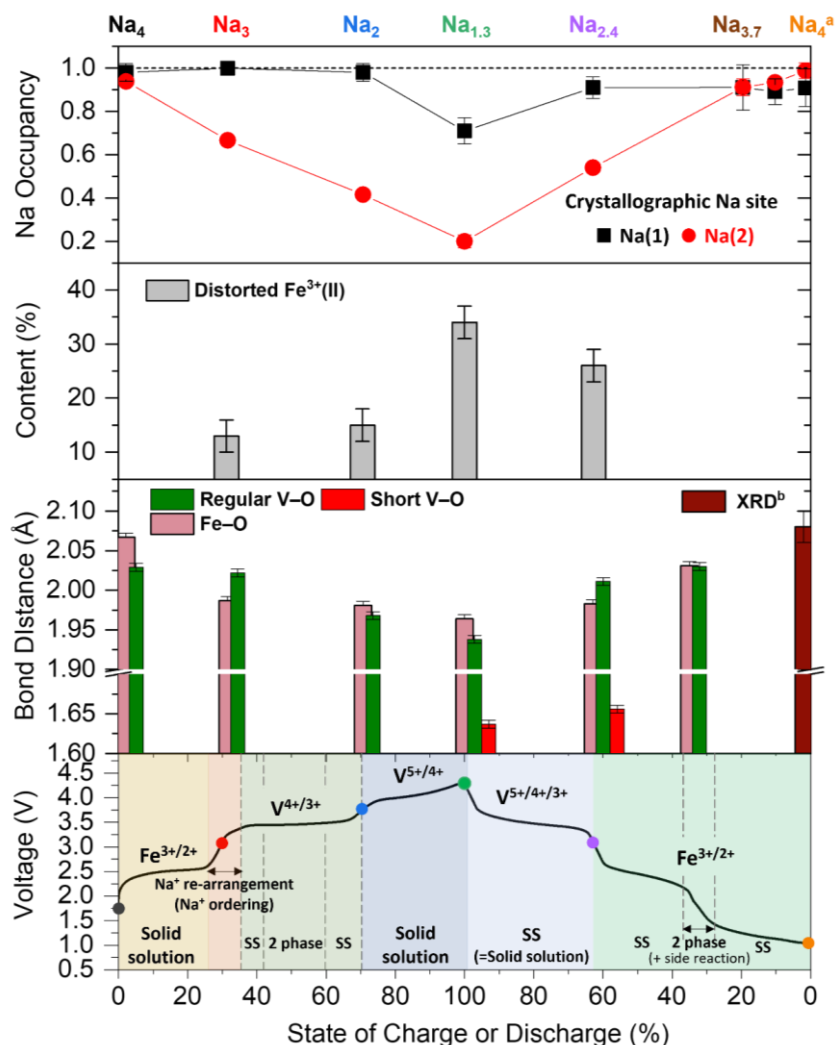
Figure 8. Global view of the asymmetric electrochemical reaction mechanism and the evolution of the Fe and V local environments including Na occupancy, distorted Fe^{3+}(II) amount, Fe – O/V – O bond distances, associated redox couples, and Na^+ extraction/insertion mechanism associated to each voltage domain during the first cycle. [a]Composition estimated from the Rietveld refinement of the structure from the XRPD pattern. [b]The value deduced from XRD analysis.

Conclusions

In conclusion, the Na^+ extraction/insertion mechanism including the asymmetric behavior induced at high voltage in a Fe/V-mixed NASICON material was comprehensively addressed based on the local and bulk point of view. Na^+ is extracted from $Na_4FeV(PO_4)_3$ through monophasic – biphasic – monophasic mechanism with three voltage domains during charge when cycled up to 4.3 V vs. Na^+/Na, and Na^+ is reinserted globally via monophasic – biphasic mechanism with

two voltage domains during discharge. Na^+ ordering in $Na_3FeV(PO_4)_3$ is observed during the Na^+ extraction process but it is not observed during the Na^+ insertion process from a highly de-sodiated $Na_{1.3}FeV(PO_4)_3$ phase. Indeed, the Na(1) site is not fully filled in discharge for that $Na_3FeV(PO_4)_3$ composition, leading thus to a disordered distribution of Na^+ ions among the two Na(1) and Na(2) sites, whereas it is fully occupied for the same composition in charge. We could assign that the three voltage domains at 2.5 V, 3.5 V, and 4.0 V during charge are associated with $Fe^{3+/2+}$, $V^{4+/3+}$, and $V^{5+/4+}$ redox couples, respectively, and the two following discharge domains at 3.4 V and 2.5 V are corresponding to the merged $V^{5+/+4/+3}$, and $Fe^{3+/2+}$ redox couples, respectively. At low voltage region and up to 3.75 V, the Fe and V local environments are found to be symmetrical but the activation of $V^{5+/4+}$ redox couple at high voltage induces the distortion of local environments with vanadyl-like short V – O bonds. The distorted Fe and V local environments are more reversible compared to other V-based NASICON compounds, although the reduction of Fe^{3+} to Fe^{2+} is hindered after the deep charge.

Supporting Information

Synchrotron powder XRD patterns, GITT curve, refined Mössbauer parameters, XANES and EXAFS spectra

Acknowledgements

References

(1)   Goodenough, J. B.; Hong, H. Y.; Kafalas, J. A. FAST Na+-ION TRANSPORT IN SKELETON STRUCTURES. *Mater. Res. Bull.* **1976**, *5* (5), 77843.

(2)   Wang, Z.; Zhong, H.; Song, G. Enhancing High-Voltage Performance of LiNi0.8Co0.1Mn0.1O2 by Coating with NASICON Fast Ionic Conductor Li1.5Al0.5Zr1.5(PO4)3. *J. Alloys Compd.* **2020**, *849*, 156467. https://doi.org/10.1016/j.jallcom.2020.156467.

(3)   Zheng, F.; Kotobuki, M.; Song, S.; Lai, M. O.; Lu, L. Review on Solid Electrolytes for All-Solid-State Lithium-Ion Batteries. *J. Power Sources* **2018**, *389* (February), 198–213. https://doi.org/10.1016/j.jpowsour.2018.04.022.

(4)   Anantharamulu, N.; Koteswara Rao, K.; Rambabu, G.; Vijaya Kumar, B.; Radha, V.; Vithal, M. A Wide-Ranging Review on Nasicon Type Materials. *J. Mater. Sci.* **2011**, *46* (9), 2821–2837. https://doi.org/10.1007/s10853-011-5302-5.

(5)   Jian, Z.; Hu, Y. S.; Ji, X.; Chen, W. NASICON-Structured Materials for Energy Storage. *Adv. Mater.* **2017**, *29* (20), 1–16. https://doi.org/10.1002/adma.201601925.

(6)   Chen, S.; Wu, C.; Shen, L.; Zhu, C.; Huang, Y.; Xi, K.; Maier, J.; Yu, Y. Challenges and Perspectives for NASICON-Type Electrode Materials for Advanced Sodium-Ion Batteries. *Adv. Mater.* **2017**, *29* (48), 1–21. https://doi.org/10.1002/adma.201700431.

(7)   Deng, Z.; Sai Gautam, G.; Kolli, S. K.; Chotard, J. N.; Cheetham, A. K.; Masquelier, C.; Canepa, P. Phase Behavior in Rhombohedral NaSiCON Electrolytes and Electrodes. *Chem. Mater.* **2020**, *32* (18), 7908–7920. https://doi.org/10.1021/acs.chemmater.0c02695.

(8)   Masquelier, C.; Croguennec, L. Polyanionic (Phosphates, Silicates, Sulfates) Frameworks as Electrode Materials for Rechargeable Li (or Na) Batteries. *Chem. Rev.* **2013**, *113* (8), 6552–6591. https://doi.org/10.1021/cr3001862.

(9)   Padhi, A. K.; Nanjundaswamy, K. S.; Masquelier, C.; Goodenough, J. B. Mapping of Transition Metal Redox Energies in Phosphates with NASICON Structure by Lithium Intercalation. *J. Electrochem. Soc.* **1997**, *144* (8), 2581–

2586. https://doi.org/10.1149/1.1837868.

(10)   Masquelier, C.; Wurm, C.; Rodríguez-Carvajal, J.; Gaubicher, J.; Nazar, L. A Powder Neutron Diffraction Investigation of the Two Rhombohedral NASICON Analogues: γ-Na3Fe2(PO4)3 and Li3Fe2(PO4)3. *Chem. Mater.* **2000**, *12* (2), 525–532. https://doi.org/10.1021/cm991138n.

(11)   Gaubicher, J.; Wurm, C.; Goward, G.; Masquelier, C.; Nazar, L. Rhombohedral Form of Li3V2(PO4)3 as a Cathode in Li-Ion Batteries. *Chem. Mater.* **2000**, *12* (11), 3240–3242. https://doi.org/10.1021/cm000345g.

(12)   Cushing, B. L.; Goodenough, J. B. Li2NaV2(PO4)3: A 3.7 V Lithium-Insertion Cathode with the Rhombohedral NASICON Structure. *J. Solid State Chem.* **2001**, *162* (2), 176–181. https://doi.org/10.1006/jssc.2001.9213.

(13)   Rajagopalan, R.; Zhang, Z.; Tang, Y.; Jia, C.; Ji, X.; Wang, H. Understanding Crystal Structures, Ion Diffusion Mechanisms and Sodium Storage Behaviors of NASICON Materials. *Energy Storage Mater.* **2021**, *34*, 171–193. https://doi.org/10.1016/J.ENSM.2020.09.007.

(14)   Zhang, J.; Liu, Y.; Zhao, X.; He, L.; Liu, H.; Song, Y.; Sun, S.; Li, Q.; Xing, X.; Chen, J. A Novel NASICON-Type Na4MnCr(PO4)3 Demonstrating the Energy Density Record of Phosphate Cathodes for Sodium-Ion Batteries. *Adv. Mater.* **2020**, *1906348*, 1–8. https://doi.org/10.1002/adma.201906348.

(15)   Wang, J.; Wang, Y.; Seo, D. H.; Shi, T.; Chen, S.; Tian, Y.; Kim, H.; Ceder, G. A High-Energy NASICON-Type Cathode Material for Na-Ion Batteries. *Adv. Energy Mater.* **2020**, *1903968*, 1–10. https://doi.org/10.1002/aenm.201903968.

(16)   Zhao, Y.; Gao, X.; Gao, H.; Dolocan, A.; Goodenough, J. B. Elevating Energy Density for Sodium-Ion Batteries through Multielectron Reactions. **2021**. https://doi.org/10.1021/acs.nanolett.1c00100.

(17)   Gao, H.; Li, Y.; Park, K.; Goodenough, J. B. Sodium Extraction from NASICON-Structured Na3MnTi(PO4)3 through Mn(III)/Mn(II) and Mn(IV)/Mn(III) Redox Couples. *Chem. Mater.* **2016**, *28* (18), 6553–6559. https://doi.org/10.1021/acs.chemmater.6b02096.

(18)   Zhu, T.; Hu, P.; Wang, X.; Liu, Z.; Luo, W.; Owusu, K. A.; Cao, W.; Shi, C.; Li, J.; Zhou, L.; Mai, L. Realizing Three-Electron Redox Reactions in NASICON-Structured Na3MnTi(PO4)3 for Sodium-Ion Batteries. *Adv. Energy Mater.* **2019**, *9* (9). https://doi.org/10.1002/aenm.201803436.

(19)   Zakharkin, M. V; Drozhzhin, O. A.; Tereshchenko, I. V; Chernyshov, D.;
       Abakumov, A. M.; Antipov, E. V; Stevenson, K. J. Enhancing Na+ Extraction
       Limit through High Voltage Activation of the NASICON-Type Na4MnV(PO4)3
       Cathode. *ACS Appl. Energy Mater.* **2018**, *1*, 5842–5846.
       https://doi.org/10.1021/acsaem.8b01269.

(20)   Chen, F.; Kovrugin, V. M.; David, R.; Mentré, O.; Fauth, F.; Chotard, J.-N.;
       Masquelier, C. A NASICON-Type Positive Electrode for Na Batteries with High
       Energy Density: $Na_4MnV(PO_4)_3$. *Small Methods* **2018**, *1800218*, 1800218.
       https://doi.org/10.1002/smtd.201800218.

(21)   de Boisse, B. M.; Ming, J.; Nishimura, S.; Yamada, A. Alkaline Excess
       Strategy to NASICON-Type Compounds towards Higher-Capacity Battery
       Electrodes. *J. Electrochem. Soc.* **2016**, *163* (7), A1469–A1473.
       https://doi.org/10.1149/2.0041608jes.

(22)   Xu, C.; Zhao, J.; Wang, E.; Liu, X. X.; Shen, X.; Rong, X.; Zheng, Q.; Ren, G.;
       Zhang, N.; Liu, X. X.; Guo, X.; Yang, C.; Liu, H.; Zhong, B.; Hu, Y. S. A Novel
       NASICON-Typed Na4VMn0.5Fe0.5(PO4)3 Cathode for High-Performance Na-
       Ion Batteries. *Adv. Energy Mater.* **2021**, *11* (22), 1–9.
       https://doi.org/10.1002/aenm.202100729.

(23)   Hadouchi, M.; Yaqoob, N.; Kaghazchi, P.; Tang, M.; Liu, J.; Sang, P.; Fu, Y.;
       Huang, Y.; Ma, J. Fast Sodium Intercalation in Na3.41£0.59FeV(PO4)3: A
       Novel Sodium-Deficient NASICON Cathode for Sodium-Ion Batteries. *Energy
       Storage Mater.* **2021**, *35* (November 2020), 192–202.
       https://doi.org/10.1016/j.ensm.2020.11.010.

(24)   Park, S.; Chotard, J. N.; Carlier, D.; Moog, I.; Courty, M.; Duttine, M.; Fauth, F.;
       Iadecola, A.; Croguennec, L.; Masquelier, C. Crystal Structures and Local
       Environments of NASICON-Type Na3FeV(PO4)3and Na4FeV(PO4)3positive
       Electrode Materials for Na-Ion Batteries. *Chem. Mater.* **2021**, *33* (13), 5355–
       5367. https://doi.org/10.1021/acs.chemmater.1c01457.

(25)   Xu, C.; Xiao, R.; Zhao, J.; Ding, F.; Yang, Y.; Rong, X.; Guo, X.; Yang, C.; Liu,
       H.; Zhong, B.; Hu, Y. S. Mn-Rich Phosphate Cathodes for Na-Ion Batteries
       with Superior Rate Performance. *ACS Energy Lett.* **2022**, *7* (1), 97–107.
       https://doi.org/10.1021/acsenergylett.1c02107.

(26)   Li, H.; Xu, M.; Long, H.; Zheng, J.; Yuan, K.; Zhang, L.; Xie, Y.; Li, S.; Gao, J.;

Lai, Y.; Zhang, Z. High-Entropy-Stabilized Polyanionic Cathodes with Multiple Redox Reactions for Sodium-Ion Battery Applications. **2022**, *PREPRINT* (available at Research Square), 1–18. https://doi.org/10.21203/rs.3.rs-1186975/v1.

(27) Mason, C. W.; Gocheva, I.; Hoster, H.; Yu, D. Y. W. Vanadium-Based Nasicon Cathode Materials with Enhanced Performance for Sodium Ion Batteries. *ECS Meet. Abstr.* **2013**, *MA2013-02* (6), 402–402. https://doi.org/10.1149/ma2013-02/6/402.

(28) Aragón, M. J.; Lavela, P.; Ortiz, G. F.; Tirado, J. L. Effect of Iron Substitution in the Electrochemical Performance of Na3V2(PO4)3 as Cathode for Na-Ion Batteries . *J. Electrochem. Soc.* **2015**, *162* (2), A3077–A3083. https://doi.org/10.1149/2.0151502jes.

(29) Fauth, F.; Peral, I.; Popescu, C.; Knapp, M. The New Material Science Powder Diffraction Beamline at ALBA Synchrotron. *Powder Diffr.* **2013**, *28* (September), S360–S370.

(30) Rodríguez-Carvajal, J. Recent Advances in Magnetic Structure Determination by Neutron Powder Diffraction. *Phys. B Phys. Condens. Matter* **1993**, *192* (1–2), 55–69. https://doi.org/10.1016/0921-4526(93)90108-I.

(31) Briois, V.; La Fontaine, C.; Belin, S.; Barthe, L.; Moreno, T.; Pinty, V.; Carcy, A.; Girardot, R.; Fonda, E. ROCK: The New Quick-EXAFS Beamline at SOLEIL. *J. Phys. Conf. Ser.* **2016**, *712* (1). https://doi.org/10.1088/1742-6596/712/1/012149.

(32) Ravel, B.; Newville, M. ATHENA, ARTEMIS, HEPHAESTUS: Data Analysis for X-Ray Absorption Spectroscopy Using IFEFFIT. *J. Synchrotron Radiat.* **2005**, *12* (4), 537–541. https://doi.org/10.1107/S0909049505012719.

(33) d'Yvoire, F.; Pintard-Scrépel, M.; Bretey, E.; de la Rochère, M. Phase Transitions and Ionic Conduction in 3D Skeleton Phosphates A3M2(PO4)3 : A = Li, Na, Ag, K ; M = Cr, Fe. *Solid State Ionics* **1983**, *9–10* (PART 2), 851–857. https://doi.org/10.1016/0167-2738(83)90101-7.

(34) Chotard, J.-N.; Rousse, G.; David, R.; Mentré, O.; Courty, M.; Masquelier, C. Discovery of a Sodium-Ordered Form of Na3V2(PO4)3 below Ambient Temperature . *Chem. Mater.* **2015**, *27* (17), 5982–5987. https://doi.org/10.1021/acs.chemmater.5b02092.

(35) Lalère, F.; Seznec, V.; Courty, M.; Chotard, J. N.; Masquelier, C. Coupled X-Ray Diffraction and Electrochemical Studies of the Mixed Ti/V-Containing NASICON: Na2TiV(PO4)3. *J. Mater. Chem. A* **2018**, *6* (15), 6654–6659. https://doi.org/10.1039/c7ta10689k.

(36) Kabbour, H.; Coillot, D.; Colmont, M.; Masquelier, C.; Mentré, O. α-Na3M2(PO4)3 (M = Ti, Fe): Absolute Cationic Ordering in NASICON-Type Phases. *J. Am. Chem. Soc.* **2011**, *133* (31), 11900–11903. https://doi.org/10.1021/ja204321y.

(37) Park, S.; Wang, Z.; Deng, Z.; Moog, I.; Canepa, P.; Fauth, F.; Carlier, D.; Croguennec, L.; Masquelier, C.; Chotard, J.-N. Crystal Structure of Na 2 V 2 (PO 4) 3 , an Intriguing Phase Spotted in the Na3V2(PO4)3 –Na1V2(PO4)3 System . *Chem. Mater.* **2021**, *2*. https://doi.org/10.1021/acs.chemmater.1c04033.

(38) Senguttuvan, P.; Rousse, G.; Dompablo, M. E. A. De; Vezin, H.; Tarascon, J.; Palacín, M. R. Supplementary Information: Low Potential Sodium Insertion in NASICON-Type Structure through the Ti (III)/ Ti (II) Redox Couple. *J. Am. Chem. Soc.* **2013**, No. Iii, 1–6.

(39) Menil, F. Systematic Trends of the 57Fe Mössbauer Isomer Shifts in (FeOn) and (FeFn) Polyhedra. Evidence of a New Correlation between the Isomer Shift and the Inductive Effect of the Competing Bond T-X ($\rightarrow$ Fe) (Where X Is O or F and T Any Element with a Formal Posit. *J. Phys. Chem. Solids* **1985**, *46* (7), 763–789. https://doi.org/10.1016/0022-3697(85)90001-0.

(40) Idczak, R.; Tran, V. H.; Świątek-Tran, B.; Walczak, K.; Zając, W.; Molenda, J. The Effects of Mn Substitution on the Structural and Magnetic Properties of the NASICON-Type Na3Fe2-XMnxPO43 Solid Solution. *J. Magn. Magn. Mater.* **2019**, *491* (July), 1–11. https://doi.org/10.1016/j.jmmm.2019.165602.

(41) Ghosh, S.; Barman, N.; Senguttuvan, P. Impact of Mg2+ and Al3+ Substitutions on the Structural and Electrochemical Properties of NASICON-NaxVMn0.75M0.25(PO4)3 (M = Mg and Al) Cathodes for Sodium-Ion Batteries. *Small* **2020**, *3*, 1–8. https://doi.org/10.1002/smll.202003973.

(42) Buryak, N. S.; Anishchenko, D. V; Levin, E. E.; Ryazantsev, S. V; Martin-diaconescu, V.; Zakharkin, M. V; Nikitina, V. A.; Antipov, E. V. High-Voltage Structural Evolution and Its Kinetic Consequences for the Na 4 MnV (PO 4) 3

Sodium-Ion Battery Cathode Material. *J. Power Sources* **2022**, *518* (August 2021), 230769. https://doi.org/10.1016/j.jpowsour.2021.230769.

(43)   Ghosh, S.; Barman, N.; Mazumder, M.; Pati, S. K.; Rousse, G.; Senguttuvan, P. High Capacity and High-Rate NASICON-Na3.75V1.25Mn0.75(PO4)3 Cathode for Na-Ion Batteries via Modulating Electronic and Crystal Structures. *Adv. Energy Mater.* **2020**, *10* (6), 1–11. https://doi.org/10.1002/aenm.201902918.

(44)   Liu, R.; Zheng, S.; Yuan, Y.; Yu, P.; Liang, Z.; Zhao, W.; Shahbazian-Yassar, R.; Ding, J.; Lu, J.; Yang, Y. Counter-Intuitive Structural Instability Aroused by Transition Metal Migration in Polyanionic Sodium Ion Host. *Adv. Energy Mater.* **2021**, *11* (3), 1–9. https://doi.org/10.1002/aenm.202003256.

(45)   Liu, R.; Xu, G.; Li, Q.; Zheng, S.; Zheng, G.; Gong, Z.; Li, Y.; Kruskop, E.; Fu, R.; Chen, Z.; Amine, K.; Yang, Y. Exploring Highly Reversible 1.5-Electron Reactions (V 3+ /V 4+ /V 5+) in Na3VCr(PO4)3 Cathode for Sodium-Ion Batteries . *ACS Appl. Mater. Interfaces* **2017**, *9* (50), 43632–43639. https://doi.org/10.1021/acsami.7b13018.

(46)   Inoishi, A.; Yoshioka, Y.; Zhao, L.; Kitajou, A.; Okada, S. Improvement in the Energy Density of Na3V2(PO4)3 by Mg Substitution. *ChemElectroChem* **2017**, *4* (11), 2755–2759. https://doi.org/10.1002/celc.201700540.

(47)   Schindler, M.; Hawthorne, F. C.; Baur, W. H. Crystal Chemical Aspects of Vanadium : Polyhedral Geometries , Characteristic Bond Valences , and Polymerization of (VO n) Polyhedra. **2000**, *II* (8), 1248–1259.

(48)   Zavalij, P. Y.; Whittingham, M. S. Structural Chemistry of Vanadium Oxides with Open Frameworks. *Acta Crystallogr. Sect. B Struct. Sci.* **1999**, *55* (5), 627–663. https://doi.org/10.1107/S0108768199004000.

TOC Graphic

Asymmetric electrochemical reaction in Fe/V-mixed NASICON

induced by the activation of V^{5+}/V^{4+} redox couple

Distorted Fe^{3+}

Velocity (mm/s)

$V^{4+/5+}$

Short V – O bond → 1.648(5) Å

Voltage (V vs. Na$^+$/Na)

x in Na$_x$FeV(PO$_4$)$_3$

Fe/V

P

Stronger O – O repulsion

Depopulated Na(1)

Na(2)